



PAPER • OPEN ACCESS

The collapse of a sonoluminescent cavitation bubble imaged with X-ray free-electron laser pulses

To cite this article: Hannes P Hoepe et al 2024 *New J. Phys.* **26** 033002

View the [article online](#) for updates and enhancements.

You may also like

- [Studies of the cavitational effects of clinical ultrasound by sonoluminescence: 3. Cavitation from pulses a few microseconds in length](#)

M J W Pickworth, P P Dendy, T G Leighton et al.

- [Molecular dynamics simulations of cavitation bubble collapse and sonoluminescence](#)

Daniel Schanz, Burkhard Metten, Thomas Kurz et al.

- [Computational simulation of ionization processes in single-bubble and multi-bubble sonoluminescence](#)

Jin-Fu Liang, , De-Feng Xiong et al.



PAPER

OPEN ACCESS

RECEIVED

22 November 2023

REVISED

1 February 2024

ACCEPTED FOR PUBLICATION

14 February 2024

PUBLISHED














5 March 2024

Original Content from
this work may be used
under the terms of the
[Creative Commons
Attribution 4.0 licence](#).

Any further distribution
of this work must
maintain attribution to
the author(s) and the title
of the work, journal
citation and DOI.



The collapse of a sonoluminescent cavitation bubble imaged with X-ray free-electron laser pulses

Hannes P Hoeppe¹ , Markus Osterhoff¹ , Atiyeh Aghel Maleki² , Juan M Rosselló^{2,3} ,
Malte Vassholz¹ , Johannes Hagemann^{4,5} , Thea Engler^{4,5} , Daniel Schwarz⁵,
Angel Rodriguez-Fernandez⁶ , Ulrike Boesenberg⁶ , Johannes Möller⁶ , Roman Shayduk⁶ ,
Jörg Hallmann⁶ , Anders Madsen⁶ , Robert Mettin²  and Tim Salditt^{1,*} 

¹ Institut für Röntgenphysik, Georg-August-Universität Göttingen, D-37077 Göttingen, Germany

² Drittes Physikalisches Institut, Georg-August-Universität Göttingen, D-37077 Göttingen, Germany

³ Faculty of Mechanical Engineering, University of Ljubljana, SVN-1000 Ljubljana, Slovenia

⁴ Helmholtz Imaging Platform, Deutsches Elektronen-Synchrotron DESY, D-22607 Hamburg, Germany

⁵ CXNS—Center for X-ray and Nano Science, Deutsches Elektronen-Synchrotron DESY, D-22607 Hamburg, Germany

⁶ European X-ray Free-Electron Laser Facility, D-22869 Schenefeld, Germany

* Author to whom any correspondence should be addressed.

E-mail: tsalditt@gwdg.de

Keywords: x-ray holography, single-bubble sonoluminescence, bubble collapse dynamics, acoustic trap, single-pulse imaging, x-ray free-electron laser

Supplementary material for this article is available [online](#)

Abstract

Single bubble sonoluminescence (SBSL) is the phenomenon of synchronous light emission due to the violent collapse of a single spherical bubble in a liquid, driven by an ultrasonic field. During the bubble collapse, matter inside the bubble reaches extreme conditions of several gigapascals and temperatures on the order of 10000 K, leading to picosecond flashes of visible light. To this day, details regarding the energy focusing mechanism rely on simulations due to the fast dynamics of the bubble collapse and spatial scales below the optical resolution limit. In this work we present phase-contrast holographic imaging with single x-ray free-electron laser (XFEL) pulses of a SBSL cavitation bubble in water. X-rays probe the electron density structure and by that provide a uniquely new view on the bubble interior and its collapse dynamics. The involved fast time-scales are accessed by sub-100 fs XFEL pulses and a custom synchronization scheme for the bubble oscillator. We find that during the whole oscillation cycle the bubble's density profile can be well described by a simple step-like structure, with the radius R following the dynamics of the Gilmore model. The quantitatively measured internal density and width of the boundary layer exhibit a large variance. Smallest reconstructed bubble sizes reach down to $R \simeq 0.8 \mu\text{m}$, and are consistent with spherical symmetry. While we here achieved a spatial resolution of a few 100 nm, the visibility of the bubble and its internal structure is limited by the total x-ray phase shift which can be scaled with experimental parameters.

1. Introduction

Collapsing bubbles in a liquid are able to focus acoustic and inertial energy to create extreme states of matter, resulting in the emission of light, when certain conditions are met. This phenomenon of sonoluminescence (SL) has been known for almost a century [1–3]. It was particularly well investigated after the discovery that pulsed light can be emitted periodically from a stable single oscillating bubble, referred to as single bubble sonoluminescence (SBSL) [4, 5]. In this scenario the bubble is trapped at the anti-node of an ultrasonic standing wave field and driven to repetitive nonlinear radial oscillations. A flash of light of less than or a few 100 ps is emitted during the first and most violent collapse of each oscillation cycle, with a spectrum close to that of a black body radiator [6–8]. Following intensive research and discussion regarding the mechanism of

SBSL and bubble oscillations, as reviewed for example in [9–11], the consensus explanation of SBSL involves adiabatic heating, dissociation and ionization of water vapour and trapped noble gases, resulting mainly in thermal bremsstrahlung from a plasma with temperatures around 10 000 K [8, 12–14].

However, some aspects of the energy focusing mechanism, such as the internal bubble structure, potentially including converging shock waves which lead to increased peak temperatures, remain elusive from an experimental point of view and rely only on numerical simulations [15–19]. Even simple parameters, such as the minimal radius to which a sonoluminescent bubble is compressed, are largely unknown. For experiments, the spatial and temporal scales of the collapse are challenging, and the bubble interior is obscured by reflection of visible light at the bubble interface. Note that the spatial scales are often at the resolution limit of rather low numerical aperture optical observations, since the acoustic standing wave fields require chambers of sufficient size and distance from a microscope objective. Particular efforts have been undertaken to resolve the final instance of collapse by pulsed [20] and streak Mie scattering [21, 22]. Since the highly compressed water surrounding the nearly collapsed bubble and later the outgoing shock wave in water are strongly optically scattering, the resolutions of these experiments were limited to about $1.7\ \mu\text{m}$ [22] to $0.7\ \mu\text{m}$ [20]. Results from both techniques suggest a spherical bubble implosion, while Weninger *et al* report possible non-spherical bubble oscillations during the re-expansion. Further, they conjecture indirect evidence for an inner shock wave, but state that a direct observation of the bubble interior is still lacking [20].

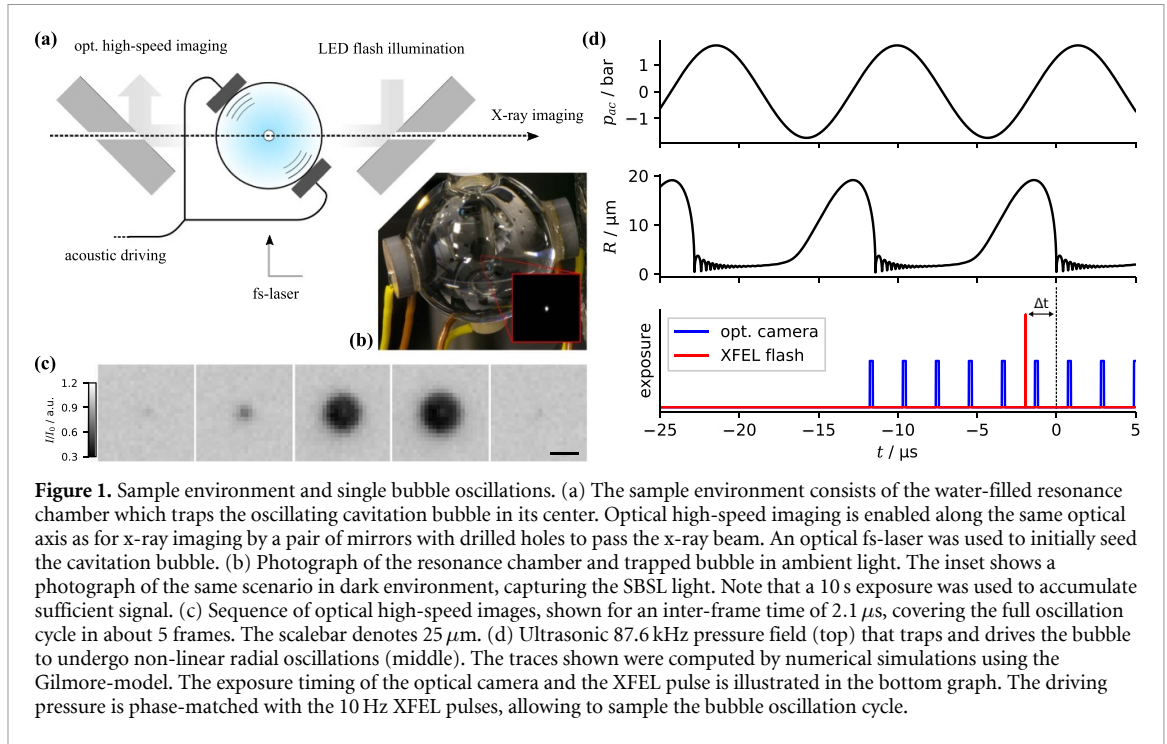
More recently, time-resolved x-ray imaging has become a valuable technique to investigate fast hydrodynamic processes [23–30], especially with the development of hard x-ray free-electron laser (XFEL) sources. A unique feature of x-ray imaging is a quantitative phase contrast mechanism, which gives direct access to the projected electron density of the sample (or mass density in case of a homogeneous object). Importantly, x-ray images also yield volumetric information of the sample structure, and are not obscured by multiple scattering, curved phase boundaries or plasma. In a preceding study, we have exploited this to investigate laser-induced cavitation and shock wave dynamics in water during the first nanoseconds after optical breakdown and with sub-micron spatial resolution [26, 31]. The time evolution of the density profile was reconstructed quantitatively across the three phase boundaries between the plasma core, the expanding bubble and the shock wave front.

In this study, we now use x-ray phase contrast imaging (PCI) with single XFEL pulses to image an acoustically trapped and sonoluminescent single cavitation bubble in water, covering the oscillation cycle and including the collapse. We implemented the experiment at the materials imaging and diffraction (MID) instrument of the European XFEL Facility in Schenefeld, Germany [32]. The required magnification is achieved by nanofocusing and recording of inline holograms in projection. By a quantitative model and least-square fitting of the observed fringes in the image, a unique tool and novel view on the bubble dynamics underlying SBSL is presented. With this approach, which is at least potentially of very high spatial and temporal resolution, we aimed at resolving the bubble at its highest states of compression, notably during the collapse. For this purpose, we have built a particularly small resonance chamber with a diameter of approximately 19 mm, and have devised a specialized synchronization scheme to phase-lock the bubble oscillator to the XFEL pulses, enabling a controlled ‘stroboscopic illumination’ experiment. Note that the XFEL pulses are so intense that single pulses can be recorded and evaluated at sufficient signal-to-noise ratio, without accumulation or averaging over successive bubble collapses. Exploiting a supposed spherical symmetry of the bubble, 1d phase reconstruction is used to yield the radial density profile and hence maximizing the sensitivity for small bubble sizes, as already demonstrated in [26] when studying laser induced cavitation.

As a result, we now obtain x-ray holograms of a (collapsing) cavitation bubble and extract the radial density profile with sub-micron spatial resolution for quasi-instantaneous snapshots recorded with ultrashort XFEL pulses. During the collapse phase, we report smallest bubble radii around $0.8\ \mu\text{m}$, based on data compatible with a spherically symmetric structure. Owing to sparse sampling and possibly only weak acoustic emission during the main bubble collapse, no compression waves are resolved. The internal density of the bubble is over-estimated especially during the afterbounces which hints at deviation from spherical symmetry. Aside from this finding, no significant direct structural difference between the violently collapsing and expanding bubble is observed, leaving some aspects related to the energy focusing mechanism still open. Finally, the potential for a increase in spatial resolution and improvements of the method to obtain details of the internal bubble structure are discussed.

2. Experimental methods

In short, phase contrast holography with single XFEL pulses was used to record a series of snapshots covering oscillation cycles of a cavitation bubble which was trapped and periodically driven by a standing ultrasound



wave. For this purpose, a custom acoustic trap setup was created which keeps the bubble in a stable position, maintaining the nonlinear oscillations for tens of minutes. An FPGA-based adaptive-frequency phase-lock system was used to synchronize the bubble oscillation to the XFEL pulses. In this way, the bubble is probed stroboscopically at a defined phase, while passing almost 8800 oscillation cycles between the consecutive XFEL pulses. By shifting the acoustic phase, the full oscillation period of the bubble dynamics was sampled.

2.1. Cavitation bubble oscillations and SBSL

The experimental setup of the sample-environment is sketched in figure 1(a). Acoustic trapping of the cavitation bubble was realized in a spherical quartz cuvette, filled with deionized and micro-pore filtered water, which was degassed for 20 min at a pressure head of 34 mbar. The water temperature is expected to be at $30^\circ\text{C} - 35^\circ\text{C}$ but could not be controlled during the experiment. A photograph of the resonator is shown in figure 1(b). The cuvette had an inner diameter of $\approx 18.8 \text{ mm}$ with a wall thickness of $\approx 360 \mu\text{m}$. Two opposite piezo-ceramic transducer discs generated an ultrasonic standing wave with an anti-node at the center of the cuvette, where the oscillating bubble was trapped. Stable oscillations and SBSL was observed at a resonance frequency of $\nu_a = 87.6 \text{ kHz}$. At the bottom of the cuvette, a piezo-ceramic receiver was used as a microphone. The acoustic driving voltage was generated by an FPGA-based signal generator, which is described in more detail in section 2.3. The signal was amplified by a linear high voltage amplifier (WMA300, Falco Systems, Netherlands) and a LC-circuit, reaching $\approx 570 \text{ V}_{\text{pp}}$ at the transducers.

Note that the cuvette size was the most critical trade-off in the design of the experiment. While typically larger resonance chambers are used in favor of the bubble's positional stability and SBSL intensity, x-ray absorption in water prompted us to keep the beam path as small as possible. After passing the quartz walls of the cuvette and the water beam path, the x-ray transmission was $\approx 11\%$. With an outer diameter of 19.5 mm the cuvette used here is, to our knowledge, the smallest resonance chamber in which SBSL has been reached so far. This is remarkable, because due to the small size the bubble is especially sensitive to any imperfections or asymmetry, such as the neck region or the arrangement of the acoustic transducers. Furthermore, the small volume of 3.5 ml of water is relatively sensitive to temperature fluctuations, either of the environment or due to x-ray and optical illumination. However, with a maximum bubble radius of $R_{\text{max}} = 18 \mu\text{m}$ (see section 3), the normalized wall distance of $d_{\text{wall}}/R_{\text{max}} \approx 520$ is sufficiently large to allow a spherical collapse. Due to the comparably small bubble size, only dim SBSL light emission was observed, which was not further quantified.

Spatial stability of the bubble oscillation was observed down to a few micrometers for the measurements presented here. Within the x-ray field of view, a translational beating motion is observed following the acoustic driving (see supplementary material). Note that the trapped bubble was observed to be mutually stable at two positions, and spontaneously jumping between those. We only captured one position in the x-ray field of view. Usually, a bubble was stable in this jumping regime for 5 to 15 min, and located at the

position of x-ray measurements approximately for 40 % of the measured cycles. The number of consecutive measurements with the bubble at this position range from 2 to 30 with a mean value of 5 measurements, corresponding to 500 ms or 44 000 oscillation cycles. During the measurements presented here, the bubble was re-seeded three times. Experimental conditions were kept almost constant, with maximum driving voltage adaptations of 0.5 % to maintain the bubble position and the oscillation regime.

2.2. Optical imaging and seeding laser

Optical high-speed imaging was employed and especially valuable to monitor the bubble oscillations during the experiment. Two drilled mirrors in front of and behind the cuvette were mounted at 45° and enabled observation coaxially with the x-ray beam (see figure 1(a)). LED flash illumination (LED P40, Kistler, Switzerland) with 10 Hz repetition and 100 μ s pulse length was used in a backlight configuration. In this way the bubble deflects the collimated light and hence appears dark in the optical images. The high-speed camera (Fastcam SAZ 2100 K, Photron, Japan) was equipped with a long-distance microscope and was continuously operated at a 10 Hz burst imaging mode, with 20 recorded frames at 480 kfps repetition rate and a shutter speed of 160 ns. In this scheme, we recorded almost 4 oscillation cycles for each XFEL pulse. Such a high-speed image series of almost one oscillation cycle is depicted in figure 1(c) and the optical burst imaging scheme, next to the stroboscopic XFEL illumination, is outlined in (d). During the anti-cycles of LED illumination, hence in darkened environment, it was possible to continuously observe SBSL with a triggered network camera. Different trigger signals, based on an XFEL master trigger, were distributed by the FPGA and delay generators (DG535, Stanford Research Systems).

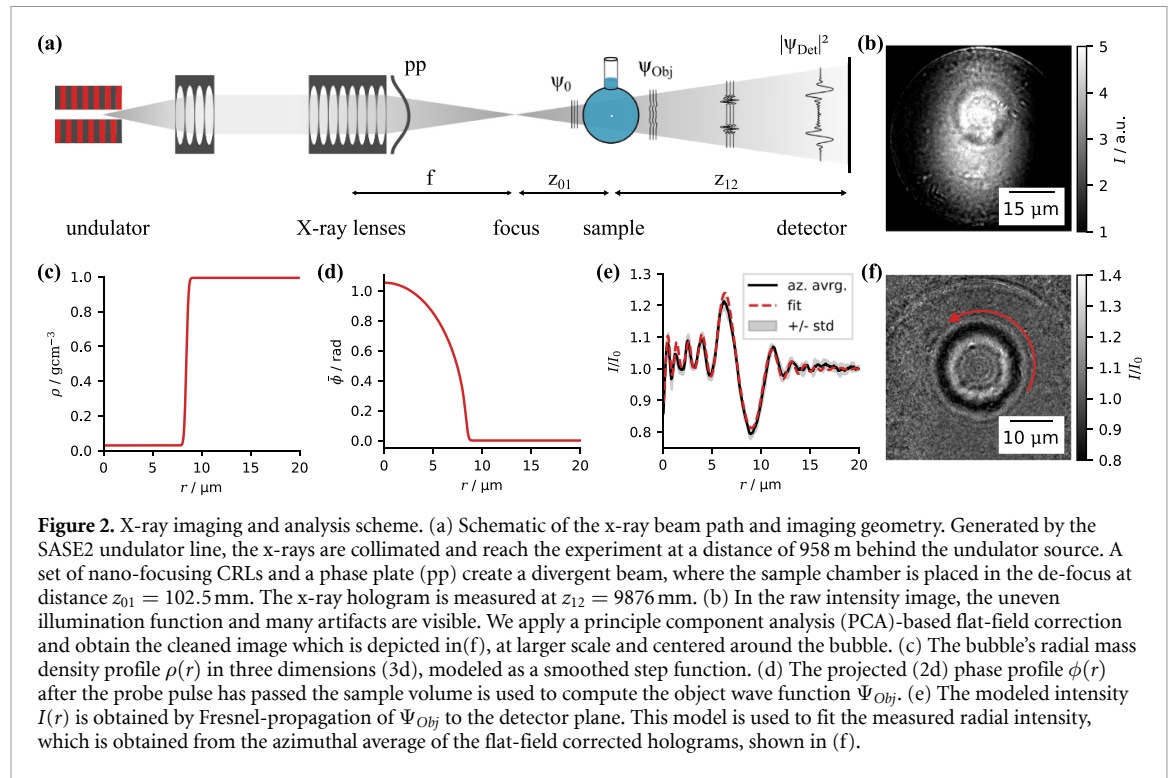
An infrared femtosecond laser was focused into the cuvette via a 90° off-axis parabolic mirror (NA \approx 0.26). This allowed us to optionally generate a new cavitation bubble with a single shot on demand, in cases where the stable oscillation was lost and the bubble dissolved. The laser was provided at the MID instrument, with a wavelength of $\lambda_l = 800$ nm and a pulse energy of approximately 56 μ J.

2.3. Synchronization by acoustic phase matching

Phase-locking of the 87.6 kHz acoustic driving and the XFEL's 10 Hz frequency was required in order to systematically sample the bubble at defined time. A main experimental challenge arose from the intrinsic (long term) jitter of the XFEL pulses with respect to the bubble oscillation. The jitter can be on the order of 100 μ s, and arises due to the synchronization of the XFEL pulse scheme to the external power grid. This was solved by a synchronization scheme which can account for the jitter of the master pulses, implemented with a custom FPGA system. The scheme is briefly described here with further details given in the supplementary material. For each XFEL pulse, the jitter was measured from a master trigger, available 17 ms before the pulse arrival. The necessary phase correction of the acoustic signal was realized by a change of the driving frequency $\nu'_a = \nu_a - \delta\nu$ for 5 ms, and then returning to ν_a for 5 ms, before the arrival of the XFEL pulse. The applied $\delta\nu$ was within the resonance width of the system. Importantly, as we show here, this adaptive frequency driving scheme still allows stable bubble oscillation and SBSL. The phase-lock resolution is estimated to be at least within a standard deviation of $\sigma_t = 26$ ns. This enabled to sample the oscillation cycle at chosen delays Δt (see figure 1(d)) and significantly narrowed the time window of the bubble collapse, in which bubbles of smallest size were recorded by random sampling. Note that the outlined synchronization scheme could easily be extended to other systems which require timing between resonant oscillators and jittery probe pulses. For example, it could possibly be used to increase the hit-rate of acoustically driven sample droplet injectors for serial femtosecond crystallography at XFELs [33].

2.4. X-ray imaging setup

Ultra-fast XFEL pulses enabled to take snapshots of the cavitation bubble dynamics in water. The x-ray imaging scheme is summarized in figure 2, with the setup sketched in (a). In-line propagation-based PCI was employed in a divergent beam geometry. In this way, x-ray holographic imaging can be performed at adjustable geometric magnification. The experiment was carried out at the MID instrument at the European XFEL [32]. The SASE2 undulator line delivered XFEL pulses with a photon energy of 18 keV, a mean pulse energy of 770 ± 150 μ J and a pulse width $\tau < 100$ fs [32]. To maximize photon flux, no monochromator was used. To measure the XFEL pulse arrival and hence optimize timing, a gas ionization chamber was placed before and, optionally, a fast diode was placed behind the sample region. At the MID instrument, the x-ray beam was focused by a set of 50 Beryllium compound refractive lenses (CRLs) [34, 35] to create a divergent beam behind the focus. The nominal focal distance was 487 mm, yielding a divergence half angle of 0.3 mrad. The sample chamber was placed at a distance $z_{01} = 102.5$ mm and the x-ray detector at a distance $z_{02} = 9876$ mm behind the focus. Air scattering was reduced by an 8 m long vacuum flight tube between the sample and the detector, which was an sCMOS camera, fibre-coupled to a LuAg scintillator (Zyla 5.5, Andor, UK). Owing to cone-beam geometry, geometrical magnification of $M = z_{02}/z_{01} = 96$ and an effective pixel



size of $px_{\text{eff}} = 71$ nm was achieved. The holographic regime is characterized by the Fresnel number $F = px_{\text{eff}}^2 M / \lambda z_{12} = 7.4 \cdot 10^{-4}$.

The contrast mechanism of PCI relies on the sample-induced distortions of the wavefront of the probing pulse. After passing the bubble chamber, the phase contrast forms during free-space propagation over the distance of several meters to the detection plane, via self-interference of the wavefunction Ψ_{Obj} behind the object [36]. In the detector plane, we recorded the intensity, i.e. the holographic image, which has formed based on wavefront distortion and self-interference. To obtain real-space information on the sample, numerical phase-reconstruction is required, or equivalently optimization of a model curve to the observed intensity pattern, as described in section 2.7.

2.5. Data collection

During the experiment at XFEL (proposal no. 2807), one day was dedicated to measurements of the oscillation and collapse of the sonoluminescent cavitation bubble (runs 138–169). We used data only from run 167 and 168 where the bubble was kept in the desired oscillation regime for about 40 min. Approximately 20 000 images were recorded, from which almost 5000 are included in the results presented here. (see supplementary material).

2.6. Image processing

For phase reconstruction, one ideally uses the knowledge of the exact illumination function. While for stable beam conditions empty-beam measurements are sufficient [37], and dedicated measurements allow to reconstruct the illumination function [38], this is not possible for single-shot imaging with XFEL pulses. Due to the stochastic nature of the self-amplification of spontaneous emission (SASE), on which the generation of (non-seeded) XFEL pulses is based, the illumination function fluctuates stochastically [25]. We therefore used a flat-field correction scheme based on PCA which was initially proposed for synchrotron radiation [39] and then was adapted for single-shot holography with XFEL pulses [25, 26]. Before each run of measurements, a set of empty images was recorded and the principle components were calculated. For each single-shot hologram, the best fitting linear combination of the principle components were computed. Figures 2(b) and (f) show an example of a raw detector image and the corresponding flat-field corrected hologram. The flat-field correction worked remarkably well and was essential for further analysis. The next key step of the analysis was the azimuthal average to increase the signal-to-noise ratio and to work with 1d radial profiles, rather than the 2d images in the following. To this end, the center of symmetry of the bubbles in each x-ray hologram was determined by a sequence of image processing steps, as described in more detail in the supplementary material.

2.7. Radial density structure fitted by forward modeling

In PCI, it is common to numerically reconstruct the two-dimensional (2d) complex-valued wave function directly behind the object (exit wave), as a way to interpret the projected electron density distribution of the object as two-dimensional images (see e.g. [37]). In this work, which considers a very simple object given by a radially symmetric bubble with a density profile $\rho(r)$, the reconstruction is carried out in the radial dimension only and implemented by a model least-square fit, based on forward propagation. This analysis scheme is conceptualized in figures 2(c)–(e). A direct comparison of the 1d and 2d reconstruction scheme is given in [26].

First, assuming spherical symmetry of the cavitation bubbles, the one-dimensional (1d) radial intensity profiles are computed by azimuthal average around the bubble center in each hologram. In this way, the signal-to-noise ratio can be increased, which is especially useful for small cavitation bubbles which are weak phase objects. The errors given by small deviations from spherical symmetry are effectively accounted for by considering the standard deviation of the azimuthal average for six angular slices of the image (gray area in figure 2(e)). A model function, described in detail below, was then used for least-square fitting of the measured intensity profiles. In this way, the phase-reconstruction reduced to a classical minimization problem with three free parameters. Each recorded hologram and the respective obtained fit parameters are interpreted as individual independent measurements of the bubble structure at the given time point.

The model function describes the 3d mass density distribution $\rho(r)$ of the cavitation bubble as a simple step profile (see figure 2(c)), implemented as a modified error function

$$\rho(r) = \rho + \frac{1}{2}(\rho_0 - \rho) \left(\operatorname{erf} \left(\frac{r - R}{\sqrt{2}\sigma_{\text{std}}} \right) + 1 \right).$$

Within the cavity, a uniform density ρ of water vapour is assumed and at the radius R , a transition layer with a FWHM $\sigma = 2\sqrt{2\ln(2)}\sigma_{\text{std}}$ forms the bubble boundary (air–water interface). Beyond the interface of the cavitation bubble, bulk equilibrium water with the density ρ_0 is assumed. Note that this model also inherently assumes a homogeneous object, i.e. a coupling of phase and absorption with constant $\kappa = \beta/\delta$ throughout the object, where β and $1 - \delta$ represent the imaginary and real components of the index of refraction of water at given photon energy and density. Correspondingly, the projected complex phase shift ϕ behind the bubble is proportional to the difference of the bubble's density distribution $\rho(r)$ and equilibrium water, integrated along the direction of the x-ray beam (see figure 2(d)). Exploiting spherical symmetry, this is implemented via the Abel transform \mathcal{A} as

$$\phi(r) = k\delta d_{\text{vx}} \mathcal{A} \left(\frac{\rho(r)}{\rho_0} - 1 \right). \quad (1)$$

Further, it is convenient to define the factor $\phi_{\text{vx,max}} = k\delta d_{\text{vx}}$ which defines the phase shift between equilibrium water and vacuum per voxel. Here $k = 2\pi/\lambda$ is the x-ray wave number, δ the real part of the x-ray refractive index of water at density ρ_0 and $d_{\text{vx}} = d_{\text{px}}/M$ the effective (magnified) voxel size. The complex object wave function is then defined as $\Psi_{\text{Obj}} = \Psi_0 \exp((i + \kappa)\phi)$ and propagated to the detector applying standard Fresnel-diffraction theory [36] to yield the intensity profile $I(r) \propto |\Psi_{\text{Det}}|^2$. Following [26] the propagation step can be written as

$$\Psi_{\text{Det}} = \exp(ik\Delta) \mathcal{H}^{-1} \mathcal{D}_{\Delta} \mathcal{H} \Psi_{\text{Obj}},$$

with the sample-detector distance Δ , the Fresnel propagation kernel $\mathcal{D}_{\Delta} = \exp\left(\frac{-i\Delta}{2k} k_{\perp}^2\right)$ and the Hankel transform \mathcal{H} , where the latter corresponds to the Fourier transformation in radial coordinates [40].

3. Results and discussion

The oscillating cavitation bubble was probed by the XFEL pulses at different time delays Δt with respect to the time of collapse. The density profile $\rho(r)$ of the bubble was reconstructed for each single-shot hologram.

Figure 3 presents a measurement series of the cavitation bubble covering the branch of the first collapse. In the center column, a set of radial intensity profiles is shown for a selected range of R and Δt , in gray. The representative bubble profile is highlighted as the solid black line. The corresponding model fit is depicted as the red dotted curve. For each profile, the flat-field corrected single-shot hologram is shown on the left, and the density distribution $\rho(r)$, as determined by the model fit, is shown on the right. For the representative bubble profiles, events were chosen with minimum least-square difference compared to the bubble model within the set of measurements.

Following the bubble on the collapse trajectory as depicted in figure 3, the bubble size decreases from $18\ \mu\text{m}$ to $1.5\ \mu\text{m}$ within $2\ \mu\text{s}$, while maintaining a spherical shape. The fringe pattern of the hologram and

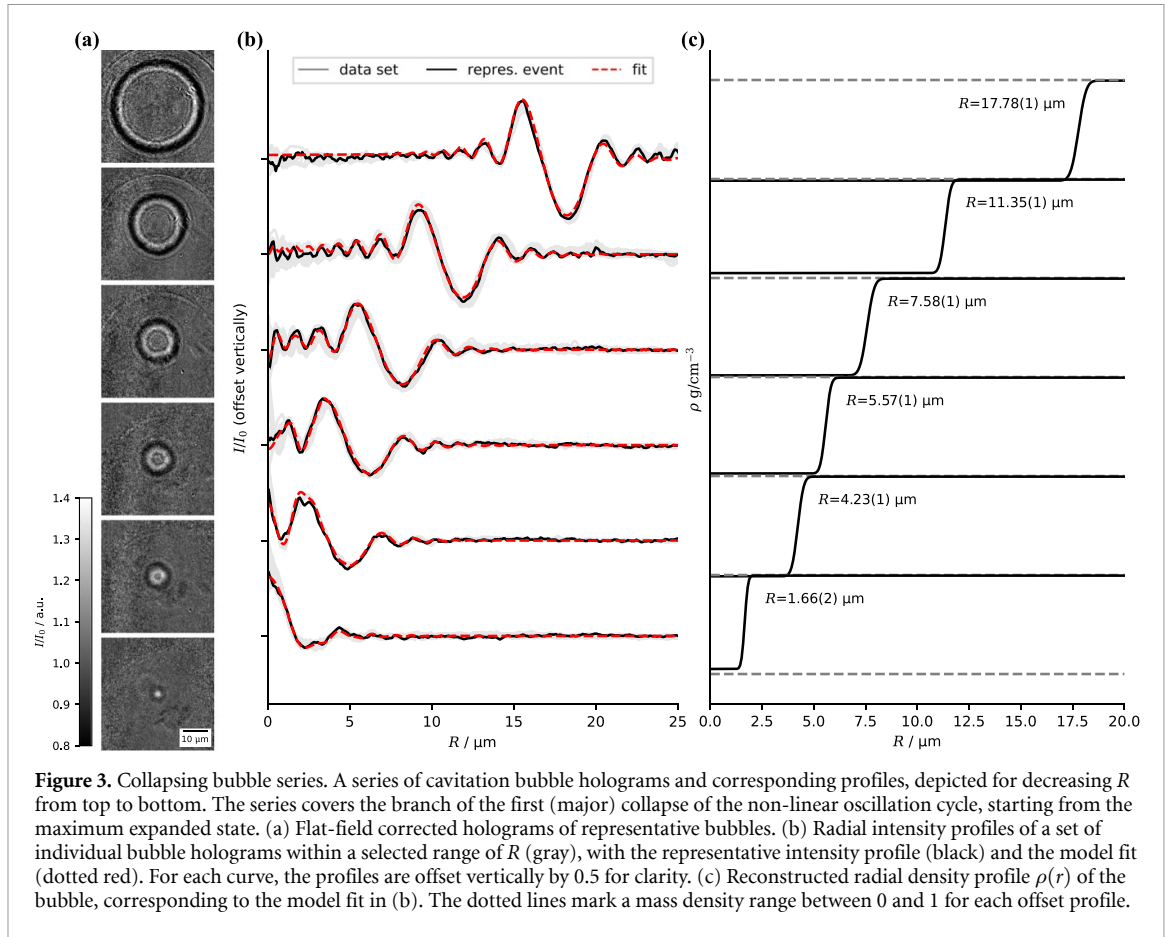


Figure 3. Collapsing bubble series. A series of cavitation bubble holograms and corresponding profiles, depicted for decreasing R from top to bottom. The series covers the branch of the first (major) collapse of the non-linear oscillation cycle, starting from the maximum expanded state. (a) Flat-field corrected holograms of representative bubbles. (b) Radial intensity profiles of a set of individual bubble holograms within a selected range of R (gray), with the representative intensity profile (black) and the model fit (dotted red). For each curve, the profiles are offset vertically by 0.5 for clarity. (c) Reconstructed radial density profile $\rho(r)$ of the bubble, corresponding to the model fit in (b). The dotted lines mark a mass density range between 0 and 1 for each offset profile.

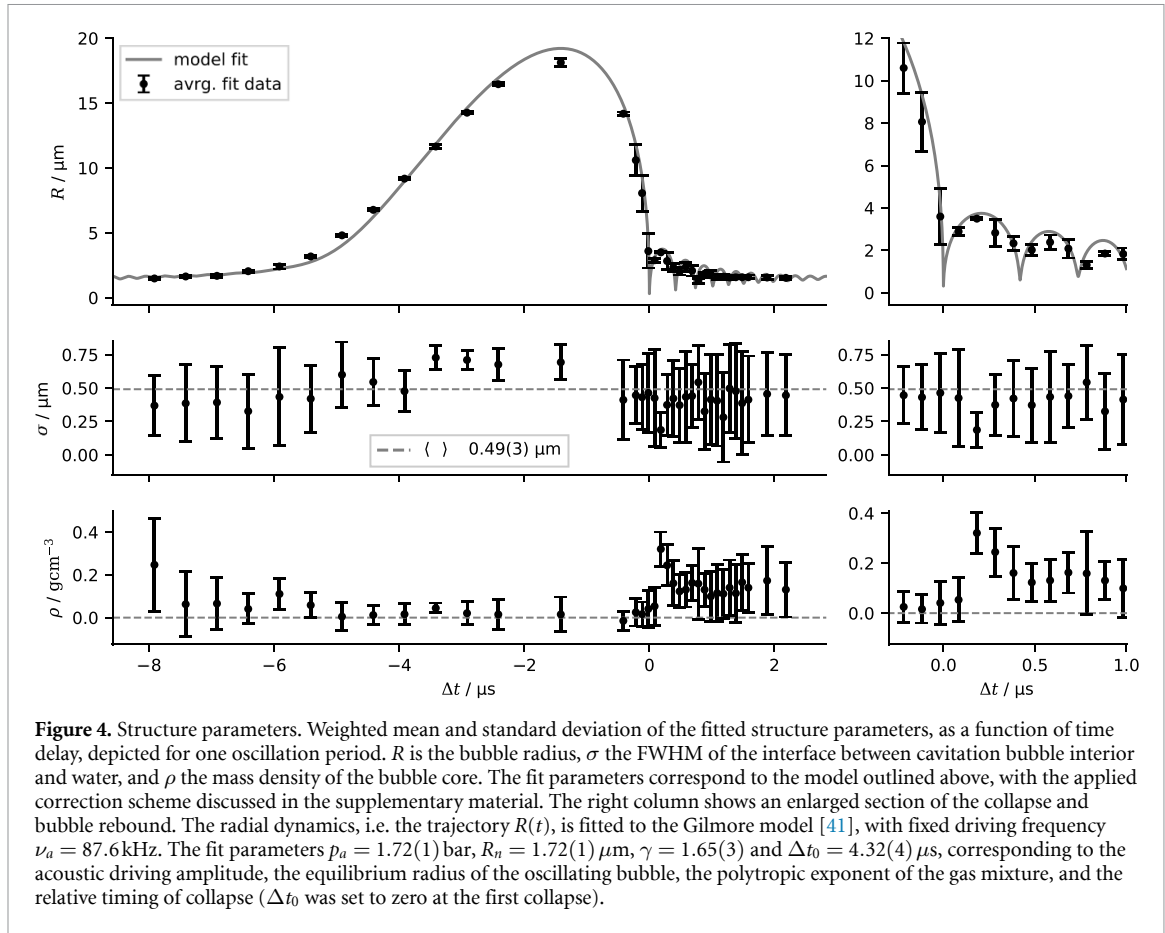
$I(r)$ changes accordingly to the bubble radius, and for large bubbles one recognizes by eye the similar fringe pattern, shifted in the radial position. For smaller bubbles, the interference pattern shows a distinct shape, with either a minimum or maximum at the center, depending on R . For all sizes, the measurements can be fitted well to the simple bubble model, indicating no fundamental change in the structure of the cavitation bubble at these stages of the dynamics. A full representation of the bubble's collapse and first rebound within the measured space of R and Δt is shown in the supplementary material in figures S8 and S7.

3.1. Fitted structure parameters

Figure 4 summarizes the fit results for all evaluated cavitation bubble holograms. The weighted mean and standard deviation of the fit parameters R , σ and ρ are plotted as a function of the delay Δt relative to the first bubble collapse. The radial dynamics $R(t)$ reflects the characteristic nonlinear oscillation of the bubble radius in the giant-response regime. The solid line describes a fit to the Gilmore model [41] with the driving frequency $\nu_a = 87.6 \text{ kHz}$ and the fit parameters $p_a = 1.72(1) \text{ bar}$, $R_n = 1.72(1) \mu\text{m}$, $\gamma = 1.65(3)$ and $\Delta t_0 = 4.32(4) \mu\text{s}$. The parameters correspond to the acoustic driving amplitude, the rest radius of the bubble, the polytropic exponent of the gas mixture, and the relative time of collapse, respectively. Further details are given in the supplementary material.

The dynamics close to the collapse is fitted best with adiabatic compression of a noble gas, i.e. $\gamma = 5/3$, indicating that mostly argon remains in the bubble during maximum compression [42]. Compared to trapped SL bubbles driven at common frequencies around 20 kHz, the fit parameters of rather high p_a and small R_n , locate the present bubble in the far upper left region of a typical $R_n - p_a$ phase space for possible stable bubble oscillations. This is in-line with previous calculations for a 100 kHz bubble, showing that for higher driving frequency the region for stable oscillations is shifted towards smaller R_n [10, 43].

The fitted radial dynamics allows to attribute single-shot holograms to different phases of the dynamics, such as the bubble expansion or collapse. After the first collapse, the rebound and the second collapse can be identified and are described well by the model. The bubble radius R can be reconstructed with high precision, indicated by low standard deviation. During the collapse, the standard deviation increases due to the fast dynamics of the bubble boundary. This indicates the timing jitter to be mainly responsible for the distribution of the radius measurement.

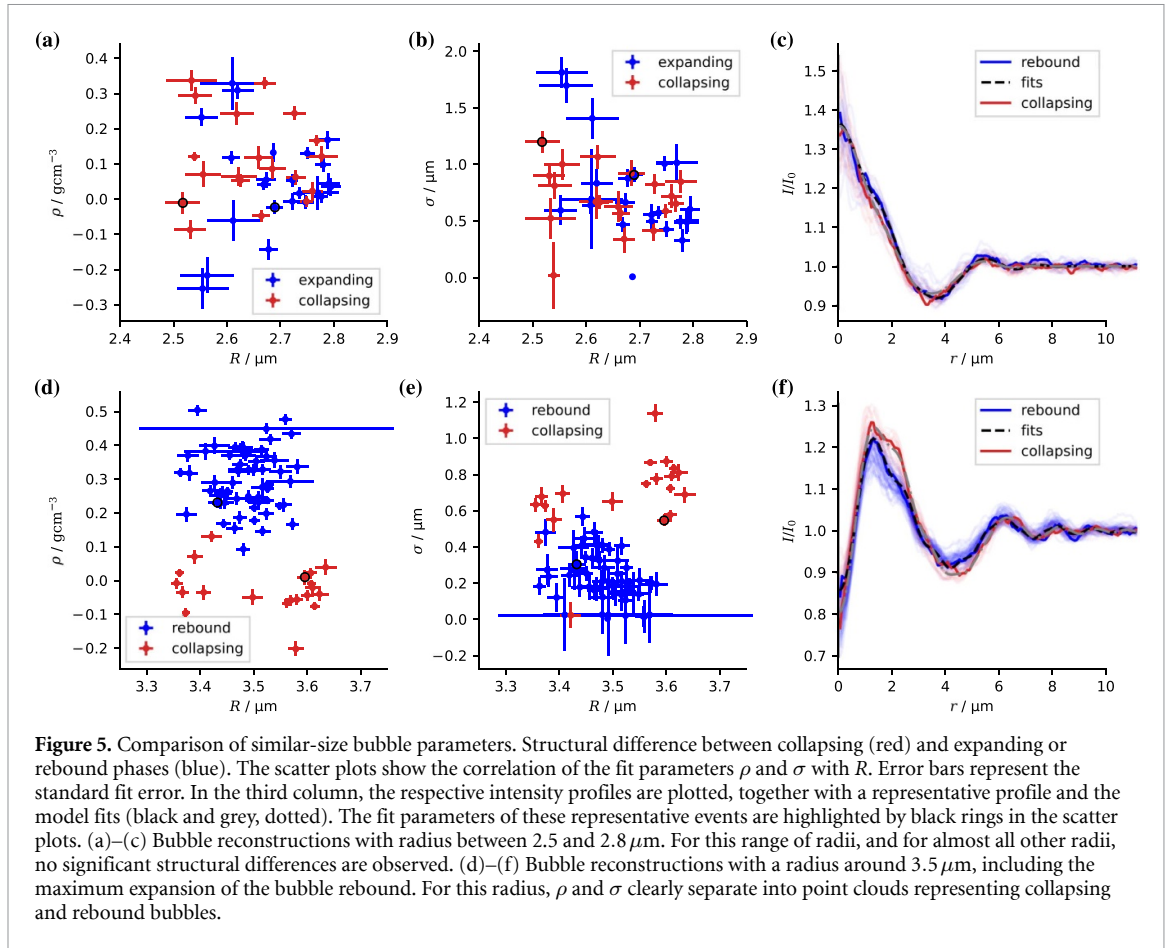


The parameter σ , which describes the FWHM of the bubble interface, exhibits large statistical errors over the whole oscillation period. Within the error bars, σ is approximately constant, with a mean value of $0.49(3) \mu\text{m}$. The local interfacial width can be expected to be microscopically small over most of the oscillation cycle, where macroscopic phase separation is warranted. Contrarily, the nature of the phase boundary during the bubble collapse is actually unclear. However, here σ accounts for all experimental effects affecting the minimum resolvable boundary width. It must hence be regarded as an experimental property rather than being a direct structure parameter of the bubble. Note that any deviation from spherical symmetry will result in finite σ , accounting for the interfacial fluctuations which could for example be described by a series expansion of spherical harmonics. Inspection of the 2d images, however, does not indicate any obvious significant deformations of the bubble, aside from imaging artifacts. In the absence of fluctuations or shape errors, the minimum edge width of the object will be inherently connected to the point spread function of the imaging setup. This resolution also depends on the coherence properties of the SASE pulses which fluctuate in their spatial and spectral composition. As a result, some density profiles can be reconstructed with a very sharp boundary while others are fitted best by a blurred profile.

The density ρ of the gas mixture in the bubble is constant and close to zero during the expansion phase, as expected for the uncompressed bubble state. Note, however, that initially this was not the case before a contrast correction scheme was applied which is described in detail in the supplementary material. The need for this correction indicated that the expected density was systematically overestimated due to a reduced contrast of the radial intensity profiles. This fact can be attributed to combined sources of experimental defects such as artifacts or coherence losses, as further discussed in the supplementary material.

Inspecting the plot of the density values (after the correction), one still observes ρ to be close to zero during the collapse dynamics, but subsequently larger than zero for smaller bubbles, while also exhibiting larger statistical errors. During maximum compression of the bubble up to 1 GPa, internal densities of 1 g cm^{-3} can be expected [11]. These peak values, however, are only reached during a very short duration of a few nanoseconds at most. Considering the timing accuracy of approx. 26 ns and sampling steps of 100 ns in this experiment, we can expect these highest compression states of the bubble to be only very weakly represented by the mean fit parameters. Single-shot measurements of smallest bubbles are further addressed in section 3.3.

A significant density peak up to almost 0.3 g cm^{-3} is observed, not at the collapse itself, but afterwards during the maximum expansion phase of the bubble rebound at $R = 3.5 \mu\text{m}$. The peak coincides with the



observation of a reduced edge width σ . Similarly, large statistical errors and an over-estimated density are observed during the bubble oscillations following the main collapse. In part, this could be explained by surface oscillations, which are expected in this regime as the deformations may arise from any instabilities during the collapse [44, 45]. In contrast to our measurements, such deformations of spherical symmetry should also result in an increase of σ . Hence, this counter-intuitive observation cannot be fully explained, and must also be attributed to systematic errors of the experiment and the analysis.

A negative correlation of σ and ρ can also be inferred from figure 4. Fits yielding a higher density at the core ρ correlate with smaller σ , and vice versa. This correlation is less pronounced for large bubbles, and highest for the bubble rebound. The corresponding correlation coefficients are -0.4 for radii between 4 – 18 μm , -0.5 for radii between 1 – 4 μm and -0.86 for radii of $3.5 \pm 0.15 \mu\text{m}$. It must be concluded, that compared to R , both σ and ρ can only be reconstructed with much larger errors of systematic origin. ρ and σ must therefore be regarded as effective parameters of the model. Contrarily, $R(t)$ is in good agreement with the spherical bubble model simulation. Notwithstanding the problems associated with ρ and σ , we can rule out strong deviations from spherical symmetry and the expected density profile. With ‘strong’ we mean major structural deviations, inconsistent even with the large error margin associated with σ and ρ .

3.2. Structure of the expanding versus the collapsing bubble phase

In a simplified picture the bubble collapse and expansion are often considered as radial dynamics with high temporal symmetry. The most prominent deviation from this symmetry is the emission of an acoustic wave (shock wave) during the collapse [46]. In addition, one could expect a difference in the density distribution of gas/vapour and liquid water in proximity of the bubble boundary [11]. Other symmetry-breaking phenomena could involve surface instabilities and bubble-breakup during collapse [10, 44]. To investigate possible structural differences of the bubble during and after the collapse, we next compare reconstructed bubbles within subsets of similar radii, which is presented in figure 5. The intensity profiles are compared as a function of r for similar R , and fit parameters are plotted as two-dimensional scatter plots in the ρ/R and σ/R planes, in order to inspect differences of collapsing (red) and expanding (rebound) phases (blue).

The results depicted in figures 5(a)–(c) confirm that, within the time window of ± 100 ns around the collapse, the bubble essentially maintains a spherical symmetry and that the same simple density profile

accounts for both collapsing and expansion phase of its dynamics. However, this can of course only be concluded for the current resolution limit, as details of the density structure during and shortly after collapse are presently not well resolved at the given signal-to-noise ratio.

An exception must be noted for bubble radii around $R = 3.5 \mu\text{m}$, shown in figures 5(d)–(f). Here, a significant structural difference is observed for the bubble during collapse, compared with the bubble rebound. This is visible as a significant separation of data points, both the structure parameters ρ and σ . Collapsing bubble states (red) are fitted best with lower core density ρ and larger σ , while the opposite is true for the rebound (blue). This difference can also be recognized by comparing the intensity profiles (figure 5(f)). The collapsing bubble phases are characterized by a higher peak intensity with a pronounced double peak, indicating low bubble density. In contrast, the bubble during rebound is characterized by stronger fringe contrast at large radial coordinate r , which is associated with a sharper interfacial boundary. The comparison shows that this effect is not an artifact of the fitting parameter, but is present in the actual data. At the same time, both states, collapsing and rebound, are still well described by the spherically symmetric bubble model.

As already discussed above, referring to figure 4(c), the density jump at the bubble rebound is not expected, as the bubble should be only compressed to high internal densities during a very short time at the collapse itself. We can hence not fully explain this counter-intuitive observation. One could expect deformations of the bubble symmetry, i.e. an after-bounce instability, during the rebound [44, 45], but this would go against the measured decrease of σ . Deformations from spherical symmetry would first result in higher σ , and then from a certain point on also results in an over-estimation of ρ . For the case of two surface harmonic modes this is further discussed in the supplementary material. Possibly also, the XFEL pulses could have ‘accidentally’ exhibited higher coherence, resulting in higher contrast and resolution during the measurements of the rebound phase. While this cannot be excluded since the delay times were not randomized, we consider this explanation to be unlikely.

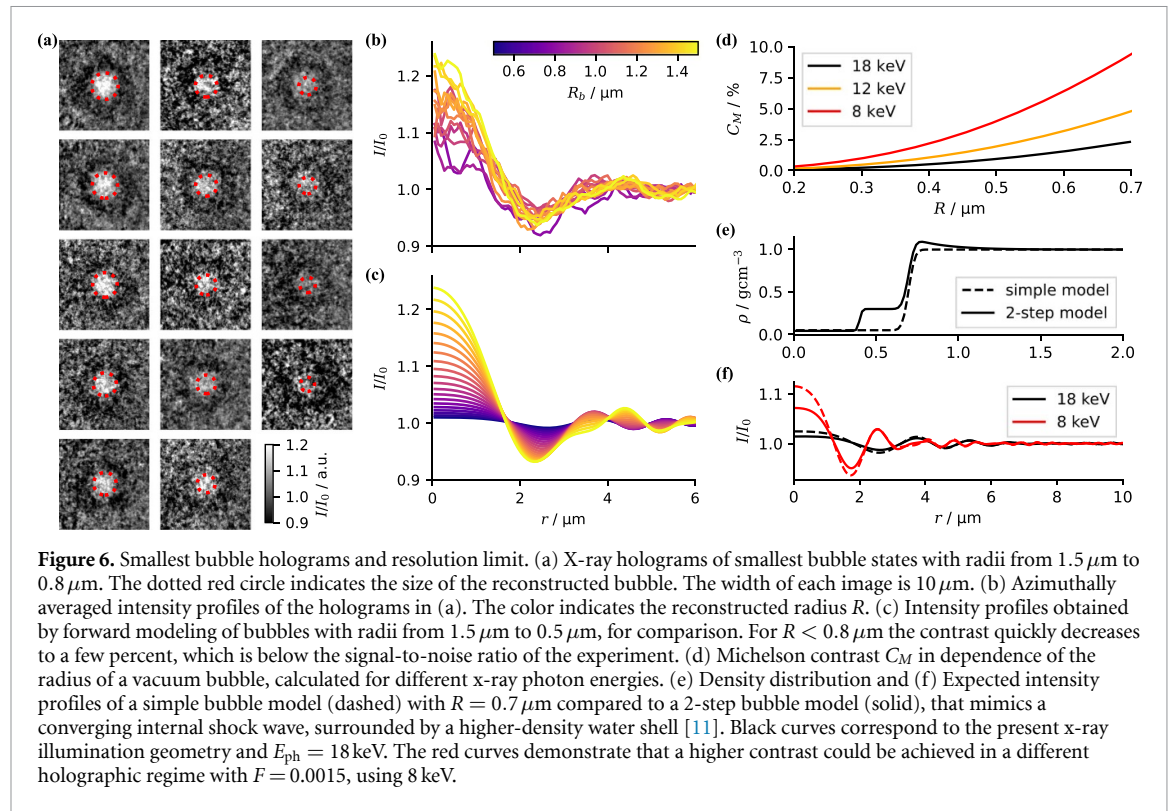
Furthermore, we conclude that the shock wave which is known to be emitted after the first collapse is not observed in our measurements. The fit of our experimental data with the Gilmore Model yields a maximum velocity of the bubble wall of 1750 ms^{-1} and a maximum pressure of 5 GPa during collapse. Previous experiments which infer on the shock pressure from velocity measurements close to the SBSL collapse report peak pressures in the range between 0.5 GPa and 6 GPa [21, 47]. Using the Tait equation of state, the respective compression of water would reached values of 1.2 g cm^{-3} to 1.5 g cm^{-3} which should be well resolved with the present signal-to-noise ratio. This is exemplified in figure S10, of the supplementary material. In addition, we have already demonstrated the capability of x-ray holographic imaging to resolve laser-induced shock wave dynamics in water [26], where shock waves with peak pressures between 1 and 14 GPa were well resolved.

The most likely explanation for the absence of shock waves in our measurements is the comparably sparse time sampling during and after the bubble collapse. A shock wave which propagates with a velocity close to the speed of sound in water of $\approx 1500 \text{ ms}^{-1}$ reaches the edge of our field of view within 10 ns. Reliable sampling of the shock propagation requires stable timing to the XFEL pulses with few nanosecond precision and is not reached with the present synchronization scheme.

3.3. Smallest bubble holograms and resolution limit

In view of our aim to resolve and investigate the smallest bubble states during the SBSL collapse, we next discuss the smallest cavitation bubbles imaged in this experiment. Figure 6(a) depicts a series of x-ray holograms of representative bubble snapshots with reconstructed radii from $1.5 \mu\text{m}$ to $0.8 \mu\text{m}$ in a quasi-linear hierarchy. The reconstructed radius R is indicated by the red dotted circle in each image. The bubble series is not a time series, but a collection of smallest bubble states recorded, from the whole oscillation cycle. While the outline of the dark fringe of the holographic object remains almost constant, the contrast reduces with R . This can also be followed by comparing the respective measured intensity profiles with the forward model intensity (figures 6(b) and (c)). Notably, spherical symmetry remains preserved for these smallest resolved bubble states.

As is shown in figure 6, the resolution-limiting factor of the present experiment is the weak total phase contrast of the bubble at smallest states, which is lost in noise. For example, a spherical bubble with $R = 0.5 \mu\text{m}$ and close-to-vacuum density exhibits a Michelson contrast $C_M < 1\%$ at 18 keV. Such a small bubble would not be visible in the present experiment. If during the maximum compression of the collapsed bubble, ρ approached values closer to the density of liquid water, the phase contrast would be reduced even further. The fit of our experimental data with the Gilmore Model predicts a minimum radius of 240 nm, clearly below the present resolution limit. The vanishing of the collapsed bubble can also be followed in figure S9 of the supplementary material.



As is discussed in detail in the supplementary material, the spatial resolution also is limited by the spectral bandwidth of the XFEL pulse, which can reduce the image contrast. For some bubble holograms however, a very sharp density profile, with $\sigma \approx px_{\text{eff}}$ is reconstructed. For these cases, it may be the case that the XFEL pulses exhibited a very narrow SASE spectrum, and consequently high coherence.

During the collapse, the bubble shape can be distorted due to Rayleigh–Taylor instabilities, jetting, or even break up into a bubble cloud [10, 44, 45]. In our measurements the bubble maintains its spherical symmetry during the first collapse and down to the smallest resolved radius. This is inline with the observation of stable spherical oscillations of the bubble, also observed by high-speed optical imaging. Although SL can occur for distorted or jetting bubbles [48], energy focusing and hence SBSL conditions should be optimal for a spherical collapse. In addition, a comparably small bubble, as is the case in the present experiment with $R_i \approx 1.7 \mu\text{m}$, is expected to be more stable against surface distortions due to surface tension and viscosity.

At the same time, surface oscillations during the after-bounces, as conjectured above, point to some initial deformations during the collapse. In addition, a systematic bubble shift is observed during collapse and rebound, relative to the expanded bubble position (see figure S11, supplementary material) This could be indicative for a jetting behaviour in the final collapse stage. A quantitative analysis of possible shape instabilities would require robust 2d reconstructions or the incorporation and fitting of spherical harmonics in the 1d reconstruction scheme. With the present signal-to-noise ratio this is not feasible, especially for smallest bubbles.

4. Summary, conclusion and outlook

We have performed x-ray holographic imaging of an oscillating cavitation bubble with single XFEL pulses. To this end, stable bubble oscillation and SBSL was realized in a particularly small resonance chamber at 87.6 kHz . A synchronization scheme was developed which phase-locks the bubble oscillation to the XFEL pulses, which are subject to jitter. We estimated the phase-lock precision to be of at least 26 ns . This has enabled controlled sampling of the full oscillation period, however, requires further improvements to reliably sample the close collapse dynamics and shock wave emission. The collapsing bubble dynamics was measured with sub-micron spatial resolution. Phase reconstruction of the 1d radial intensity profiles enabled a precise measurement of the bubble radius. The internal density ρ as well as the effective width of the bubble boundary σ can be determined, but must be regarded as effective parameters which also account for remaining inaccuracies. The low signal-to-noise ratio associated with the small phase shifts for a photon energy of 18 keV and the SASE fluctuation of the pulse spectrum and illumination function pose further

limitations. Notwithstanding these persistent challenges, structural integrity and spherical symmetry can be reported for the bubble collapse phase, down to a radius of $0.8\ \mu\text{m}$. This result is in line with the widely accepted concept of homogeneous adiabatic compression during the collapse. At the same time, the visibility of the bubble with smaller sizes during the instant of the first collapse is limited due to its vanishing phase contrast. Similarly, a possible more complex density distribution during the fast collapse dynamics, as well as the shock wave emission, remains unresolved at the present signal-to-noise ratio.

We have demonstrated that x-ray imaging enables a unique view on the cavitation bubble collapse, which is one of the most difficult hydrodynamic phenomena to access experimentally. In future experiments a narrower spectrum and improved imaging conditions may allow us to reach sensitivity to bubble states deeper in sub-micrometer scale. To this end, upcoming seeded XFEL operation [49–51] is particularly promising.

Since resolution and visibility are mainly limited by the signal-to-noise ratio, a smaller experimental chamber compatible with lower photon energy and hence a larger phase shift is the most promising route towards better results. Lower photon energies would also allow for stronger focusing power of the CRLs, such that with a reduced propagation distance z_{12} a different holographic regime is reached, while maintaining the same FOV and geometric magnification. These combined effects of lower photon energy on the contrast are compared in figures 6(d)–(f). Compared to the present experimental setting using $E_{\text{ph}} = 18\text{ keV}$ (black), a bubble with homogeneous density and $R = 0.7\ \mu\text{m}$ (dashed) leads to a comfortable contrast at 8 keV.

Of particular interest are deviations from a simple bubble structure during the bubble collapse. As proposed by e.g. [15, 16, 22] and indicated by molecular dynamics simulation [19], converging pressure or shock waves could lead to a compressed high-density bubble core, reaching much higher pressure and temperature than a bubble with continuous internal density distribution. In figures 6(e) and (f), the signal for a hypothetical density profile of a bubble including an internal converging shock wave (solid), implemented as a two-step model, is compared to the signal of the single-step model (dashed). The minor difference between both bubble holograms is beyond the current resolution limit by approximately one order of magnitude, but may be reached given the above outlined scaling of experimental parameters. As a further example, the scenario of a converged shock wave is shown in figure S10 of the supplementary material.

With a smaller spherical cuvette as a requirement for an improvement of contrast, however, the proximity of the walls makes it more difficult to achieve stable trapping or a spherical collapse and with that reaching SBSL. Alternative geometries which minimize the x-ray path through water in one direction have been explored but stable trapping was not (yet) possible. The outlined imaging setting could also be used to investigate the collapse of laser-induced bubbles [52], bubble collapse and SL in a water hammer device [53] or to resolve bulk nanobubbles [54] beyond the current limits.

With the results of this work and the discussed experimental improvements, holography with single XFEL pulses offers a novel perspective for smallest bubbles and a possibly complex density structure during the collapse of sonoluminescent bubbles.

Data availability statement

The data that support the findings of this study will be openly available following an embargo at the following URL/DOI: <https://doi.org/10.22003/XFEL.EU-DATA-002807-00>. Data will be available from 17 October 2024 [55].

Acknowledgments

We thank P Luley for engineering support, A v Roden-Wendhausen for fabrication of the glass cuvettes and S Bahl and M Schönekeß for electronics work and support. We further thank Bruno Fernandes (European XFEL, EEE, Fast Electronics) for support. We acknowledge European XFEL in Schenefeld, Germany, for provision of XFEL beamtime at MID and would like to thank the staff for their assistance. We acknowledge BMBF as a principal fund for this work through project 05K22MG2 ‘ULFAHOL: Weiterentwicklung der Vollfeldbildgebungsmethode durch inline-Holographie am Instrument MID des European XFEL’. Further we acknowledge SFB 1456/C03 for additional support. M V and T S are members of the Max-Planck School of Photonics. A A and R M gratefully acknowledge support by the German Research Foundation, DFG grant Me 1645/5-2. This research was supported in part through the Maxwell computational resources operated at DESY. We acknowledge funding of the nanofocusing setup at MID through BMBF projects 05K13OD2 ‘Erzeugung und Charakterisierung von nanofokussierten XFEL-Pulsen zur Abbildung ultraschneller Prozesse in Materie’. Finally, we thank VKT GmbH for providing the high-speed camera and Kistler Group for providing the flash LED during the experiment.

ORCID iDs

Hannes P Hoeppe  <https://orcid.org/0000-0002-4341-5121>
 Markus Osterhoff  <https://orcid.org/0000-0002-7865-515X>
 Atiyeh Aghel Maleki  <https://orcid.org/0009-0001-8771-1707>
 Juan M Rosselló  <https://orcid.org/0000-0001-7005-9452>
 Malte Vassholz  <https://orcid.org/0000-0002-0368-8782>
 Johannes Hagemann  <https://orcid.org/0000-0003-2768-9496>
 Thea Engler  <https://orcid.org/0009-0006-8183-3603>
 Angel Rodriguez-Fernandez  <https://orcid.org/0000-0003-0587-5263>
 Ulrike Boesenberg  <https://orcid.org/0000-0002-1195-6329>
 Johannes Möller  <https://orcid.org/0000-0001-8363-9077>
 Roman Shayduk  <https://orcid.org/0000-0002-3577-8918>
 Jörg Hallmann  <https://orcid.org/0000-0002-1996-397X>
 Anders Madsen  <https://orcid.org/0000-0001-6594-1029>
 Robert Mettin  <https://orcid.org/0000-0003-1780-5131>
 Tim Salditt  <https://orcid.org/0000-0003-4636-0813>

References

- [1] Frenzel H and Schultes H 1934 Lumineszenz im ultraschallbeschiedten wasser *Z. Phys. Chem.* **27B** 421–4
- [2] Putterman S J and Weninger K R 2000 Sonoluminescence: how bubbles turn sound into light *Annu. Rev. Fluid Mech.* **32** 445–76
- [3] Ronald Young F 2004 *Sonoluminescence* (CRC Press)
- [4] Barber B P and Putterman S J 1991 Observation of synchronous picosecond sonoluminescence *Nature* **352** 318–20
- [5] Felipe Gaitan D, Crum L A, Church C C and Roy R A 1992 Sonoluminescence and bubble dynamics for a single, stable, cavitation bubble *J. Acoust. Soc. Am.* **91** 3166–83
- [6] Hiller R, Putterman S J and Barber B P 1992 Spectrum of synchronous picosecond sonoluminescence *Phys. Rev. Lett.* **69** 1182–4
- [7] Hiller R A, Putterman S J and Weninger K R 1998 Time-resolved spectra of sonoluminescence *Phys. Rev. Lett.* **80** 1090–3
- [8] Hilgenfeldt S, Grossmann S and Lohse D 1999 Sonoluminescence light emission *Phys. Fluids* **11** 1318–30
- [9] Brenner M P, Hilgenfeldt S and Lohse D 2002 Single-bubble sonoluminescence *Rev. Mod. Phys.* **74** 425–84
- [10] Lauterborn W and Kurz T 2010 Physics of bubble oscillations *Rep. Prog. Phys.* **73** 106501
- [11] Lauterborn W, Kurz T and Akhatov I 2014 Nonlinear acoustics in fluids *Springer Handbook of Acoustics, Springer Handbooks* ed D R Thomas (Springer) pp 265–314
- [12] Yasui K 1999 Mechanism of single-bubble sonoluminescence *Phys. Rev. E* **60** 1754–8
- [13] Puente G F, Urteaga R and Bonetto F J 2005 Numerical and experimental study of dissociation in an air-water single-bubble sonoluminescence system *Phys. Rev. E* **72** 046305
- [14] Flannigan D J and Suslick K S 2005 Plasma formation and temperature measurement during single-bubble cavitation *Nature* **434** 52–55
- [15] Wu C C and Roberts P H 1993 Shock-wave propagation in a sonoluminescing gas bubble *Phys. Rev. Lett.* **70** 3424–7
- [16] Moss W C, Clarke D B, White J W and Young D A 1994 Hydrodynamic simulations of bubble collapse and picosecond sonoluminescence *Phys. Fluids* **6** 2979–85
- [17] Vuong V Q, Szeri A J and Young D A 1999 Shock formation within sonoluminescence bubbles *Phys. Fluids* **11** 10–17
- [18] Lauterborn W, Kurz T, Metten B, Geisler R and Schanz D 2004 Molecular dynamics approach to sonoluminescent bubbles *Theoretical and Computational Acoustics 2003* (World Scientific) pp 233–43
- [19] Schanz D, Metten B, Kurz T and Lauterborn W 2012 Molecular dynamics simulations of cavitation bubble collapse and sonoluminescence *New J. Phys.* **14** 113019
- [20] Weninger K R, Barber B P and Putterman S J 1997 Pulsed mie scattering measurements of the collapse of a sonoluminescing bubble *Phys. Rev. Lett.* **78** 1799–802
- [21] Pecha R and Gompf B 2000 Microimplosions: cavitation collapse and shock wave emission on a nanosecond time scale *Phys. Rev. Lett.* **84** 1328–30
- [22] Gompf B and Pecha R 2000 Mie scattering from a sonoluminescing bubble with high spatial and temporal resolution *Phys. Rev. E* **61** 5253–6
- [23] Vagovič P et al 2019 Megahertz x-ray microscopy at x-ray free-electron laser and synchrotron sources *Optica* **6** 1106–9
- [24] Zhang G, Khelifa I, Fezzaa K, Ge M and Coutier-Delgosha O 2020 Experimental investigation of internal two-phase flow structures and dynamics of quasi-stable sheet cavitation by fast synchrotron x-ray imaging *Phys. Fluids* **32** 113310
- [25] Hagemann J et al 2021 Single-pulse phase-contrast imaging at free-electron lasers in the hard x-ray regime *J. Synchrotron Radiat.* **28** 52–63
- [26] Vassholz M et al 2021 Pump-probe x-ray holographic imaging of laser-induced cavitation bubbles with femtosecond FEL pulses *Nat. Commun.* **12** 3468
- [27] Vassholz M et al 2023 Structural dynamics of water in a supersonic shockwave *Phys. Fluids* **35** 016126
- [28] Bokman G T, Biasiori-Poulanges L, Lukić B, Bourquard C, Meyer D W, Rack A and Supponen O 2023 High-speed x-ray phase-contrast imaging of single cavitation bubbles near a solid boundary *Phys. Fluids* **35** 013322
- [29] Xiang K 2023 Ultrasound cavitation and exfoliation dynamics of 2d materials re-vealed in operando by x-ray free electron laser megahertz imaging (arXiv:2305.08538)
- [30] Rosselló J M et al 2024 Jetting bubbles observed by x-ray holography at a free-electron laser: Internal structure and the effect of non-axisymmetric boundary conditions *Exp. Fluids* **65** 20
- [31] Osterhoff M et al 2021 Nanosecond timing and synchronization scheme for holographic pump-probe studies at the MID instrument at European XFEL *J. Synchrotron Radiat.* **28** 987–94

- [32] Madsen A 2021 Materials Imaging and Dynamics (MID) instrument at the European x-ray Free-Electron Laser Facility *J. Synchrotron Radiat.* **28** 2021
- [33] Echelmeier A, Sonker M and Ros A 2019 Microfluidic sample delivery for serial crystallography using XFELs *Anal. Bioanal. Chem.* **411** 6535–47
- [34] Lengeler B, Schroer C G, Kuhlmann M, Benner B, Günzler T F, Kurapova O, Zontone F, Snigirev A and Snigireva I 2005 Refractive x-ray lenses *J. Phys. D: Appl. Phys.* **38** A218
- [35] Seiboth F et al 2020 Hard x-ray wavefront correction via refractive phase plates made by additive and subtractive fabrication techniques *J. Synchrotron Radiat.* **27** 1121–30
- [36] Paganin D 2006 *Coherent X-ray Optics* (OUP Oxford)
- [37] Bartels M, Krenkel M, Haber J, Wilke R N and Salditt T 2015 X-ray holographic imaging of hydrated biological cells in solution *Phys. Rev. Lett.* **114** 048103
- [38] Schropp A et al 2013 Full spatial characterization of a nanofocused x-ray free-electron laser beam by ptychographic imaging *Sci. Rep.* **3** 1633
- [39] Van Nieuwenhove V, De Beenhouwer J, De Carlo F, Mancini L, Marone F and Sijbers J 2015 Dynamic intensity normalization using eigen flat fields in x-ray imaging *Opt. Express* **23** 27975–89
- [40] Baddour N 2009 Operational and convolution properties of two-dimensional fourier transforms in polar coordinates *J. Opt. Soc. Am. A* **26** 1767–77
- [41] Gilmore, F R 1952 The Growth or Collapse of a Spherical Bubble in a viscous Compressible Liquid. *Hydrodynamics Laboratory California Institute of Technology*, Report No. 26-4
- [42] Lohse D, Brenner M P, Dupont T F, Hilgenfeldt S and Johnston B 1997 Sonoluminescing air bubbles rectify argon *Phys. Rev. Lett.* **78** 1359–62
- [43] Koch P, Kurz T, Parlitz U and Lauterborn W 2011 Bubble dynamics in a standing sound field: the bubble habitat *J. Acoust. Soc. Am.* **130** 3370–8
- [44] Hilgenfeldt S, Lohse D and Brenner M P 1996 Phase diagrams for sonoluminescing bubbles *Phys. Fluids* **8** 2808–26
- [45] Bogoyavlenskiy, V A 2000 Single-bubble sonoluminescence: shape stability analysis of collapse dynamics in a semianalytical approach *Phys. Rev. E* **62** 2158–67
- [46] Matula T J, Hallaj I M, Cleveland R O, Crum L A, Moss W C and Roy R A 1998 The acoustic emissions from single-bubble sonoluminescence *J. Acoust. Soc. Am.* **103** 1377–82
- [47] Holzfuss J, Rüggeberg M and Billo A 1998 Shock wave emissions of a sonoluminescing bubble *Phys. Rev. Lett.* **81** 5434–7
- [48] Cairós C and Mettin R 2017 Simultaneous high-speed recording of sonoluminescence and bubble dynamics in multibubble fields *Phys. Rev. Lett.* **118** 064301
- [49] Amann J et al 2012 Demonstration of self-seeding in a hard-x-ray free-electron laser *Nat. Photon.* **6** 693–8
- [50] Nam I et al 2021 High-brightness self-seeded x-ray free-electron laser covering the 3.5 keV to 14.6 keV range *Nat. Photon.* **15** 435–41
- [51] Liu S et al 2023 Cascaded hard x-ray self-seeded free-electron laser at megahertz repetition rate *Nat. Photon.* **17** 984–91
- [52] Englert E, Mccarn A and Williams G 2011 Luminescence from laser-induced bubbles in water-glycerol mixtures: effect of viscosity *Phys. Rev. E* **83** 046306
- [53] Urteaga R, Luis García-Martínez P and Bonetto F J 2009 Dynamics of sonoluminescing bubbles within a liquid hammer device *Phys. Rev. E* **79** 016306
- [54] Rosselló J M and Ohl C-D 2021 On-Demand bulk nanobubble generation through pulsed laser illumination *Phys. Rev. Lett.* **127** 044502
- [55] Salditt T 2021 Cavitation Dynamics Studied by Time-Resolved High-Resolution X-ray Holography: Bubble Nucleation and Bubble Collapse *European XFEL proposal 2807* (<https://doi.org/10.22003/XFEL.EU-DATA-002807-00>)